remote sensing

MDPI

*Article*

# Identification Method for Spring Dust Intensity Levels Based on Multiple Remote Sensing Parameters

**Qi Jiang [1], Linchang An [1], Fei Wang [2,*], Guozhou Wu [3], Jianwei Wen [4], Bin Li [5], Yuchen Jin [3] and Yapeng Wei [6]**

[1] National Meteorological Centre, Beijing 100081, China; jiangqi89@163.com (Q.J.); anlch@cma.gov.cn (L.A.)
[2] CMA Key Laboratory of Cloud-Precipitation Physics and Weather Modification (CPML), CMA Weather Modification Centre (WMC), Beijing 100081, China
[3] Inner Mongolia Institute of Meteorological Sciences, Hohhot 010051, China
[4] Inner Mongolia Meteorological Information Center, Hohhot 010051, China
[5] Inner Mongolia Ecological and Agricultural Meteorological Center, Hohhot 010051, China
[6] Jiu Quan Meteorological Administration, Jiuquan 735000, China
* Correspondence: feiwang@cma.gov.cn

**Abstract:** The advancement of more precise remote sensing inversion technology for dust aerosols has long been a hot topic in the field of the atmospheric environment. In 2023, China experienced 18 dust-related weather events, predominantly in spring. These high-intensity and frequent dust events have attracted considerable attention. However, gridded observation data of dust intensity levels are not collected in current dust monitoring and forecasting operations. Based on the Himawari 9 geostationary satellite data, this study establishes a new method to identify spring dust events. This method integrates the brightness temperature difference method and the multiple infrared dust index, taking into account the response discrepancies of the multiple infrared dust index under various underlying surfaces. Furthermore, by obtaining dynamic background brightness temperature values eight times a day, threshold statistics are applied to analyze the correlation between the infrared difference dust index and ground-observed dust level, so as to establish a satellite-based near-surface dust intensity level identification algorithm. This algorithm aims to improve dust detection accuracy, and to provide more effective gridded observation support for dust forecasting and monitoring operations. The test results indicate that the algorithm can effectively identify the presence or absence of dust, with a misjudgment rate of less than 3%. With regard to dust intensity, the identification of blowing sand and floating dust aligns relatively well with ground-based observations, but notable uncertainties exist in determining a dust intensity of sand-storm level or above. Among these uncertainties, the differences between ground-based observations and satellite identification caused by non-grounded dust in the upper air, and the selection of dust identification thresholds, are two important error sources in the dust identification results of this study.

**Keywords:** dust intensity level; brightness temperature; multispectral; underlying surface; Himawari 9

check for updates

**Citation:** Jiang, Q.; An, L.; Wang, F.; Wu, G.; Wen, J.; Li, B.; Jin, Y.; Wei, Y. Identification Method for Spring Dust Intensity Levels Based on Multiple Remote Sensing Parameters. *Remote Sens.* **2024**, *16*, 2606. https://doi.org/10.3390/rs16142606

Academic Editor: Carmine Serio

Received: 11 June 2024
Revised: 11 July 2024
Accepted: 12 July 2024
Published: 17 July 2024

## 1. Introduction

Dust aerosols are one of the most crucial components of tropospheric aerosols [1], which can trigger complex forcing and feedback mechanisms within the Earth system [2]. Dust aerosols can affect the radiative energy balance of the atmosphere–Earth system through direct effects [3–5] and indirect effects by serving as cloud condensation nuclei or ice nuclei [6,7]. As significant absorptive aerosols, dust aerosols can absorb solar radiation and release it as thermal radiation, causing non-adiabatic heating of the atmosphere [8]. Additionally, dust deposited on the ground can increase the surface temperature through the 'dark snow' effect', accelerating snowmelt and glacier retreat [3,9]. Furthermore, dust is important in the biogeochemical cycle [10,11]. It may provide a wealth of trace elements to terrestrial vegetation and marine microorganisms [12], thereby impacting the global carbon cycle directly and indirectly.

The arid and semi-arid regions in northwestern China are some of the major sources of dust aerosols in East Asia [13]. However, due to the limited number and uneven distribution of ground-based observation stations, obtaining comprehensive information on the sources and transportation of dust aerosols is challenging. Satellite remote sensing, especially the systematic monitoring of geostationary satellites, has emerged as an ideal tool for studying the spatial–temporal distribution and transport characteristics of dust aerosols. The mainstream methods for satellite dust identification can be classified into four categories: visible light–near-infrared, ultraviolet, thermal infrared, and passive microwave.

Shortwave reflectance observations are widely used in dust radiative forcing and aerosol retrieval [14–16], but they are highly uncertain over deserts due to the influence of surface reflection [17]. The microwave polarization brightness temperature difference index proposed by Huang et al. [4] enables the identification of dust under partial cloud cover. Yet, existing microwave sensors, mostly carried by polar-orbiting satellites, often lack the spatial and temporal resolution necessary for monitoring the dynamic evolution of dust. Thermal infrared observations are mainly influenced by slowly varying factors such as atmospheric temperature profiles, surface temperature, and surface emissivity, which is conducive to the quantitative inversion of dust aerosols over high-reflectance surfaces during nighttime [18,19]. The infrared difference dust index (IDDI) method [20] and brightness temperature difference (BTD) method [21] are commonly used in the infrared remote sensing detection of dust aerosols. Among them, the BTD method typically employs fixed thresholds for dust identification, with the continuously evolution of various combinations of brightness temperature differences, namely BTD (11–12), BTD (3–11), and BTD (8–11) [21–23]. These BTD methods have different thresholds, such as less than 0 or $-0.5$. For instance, Park et al. [24] and Zhang et al. [25] proposed static meteorological satellite dust remote sensing monitoring algorithms based on dynamic thresholds by establishing a clear-sky BTD (11–12) background field.

Additionally, various dust indexes were suggested for dust identification. The normalized difference dust index (NDDI) based on MODIS reflectance bands 3 and 7 was suggested by Qu et al. [14], and values larger than 0.28 indicate dust. The threshold value is subject to considerable uncertainty, and the dust thresholds for 2009 and 2010 have been adjusted accordingly to a range of $-0.05$ to 0.3 and higher than $-0.05$, respectively [22]. The Middle East dust index (MEDI) was used to highlight the difference between dust and desert surfaces, and values larger than 0.6 indicate dust [26]. The thermal infrared (TIR) dust index, which uses the brightness temperature of MODIS bands 20, 30, 31, and 32, was presented by Hao and Qu [27], and values higher than 0.28 indicate a dust region. In recent years, efforts have been focused on the comprehensive remote sensing identification of dust based on multi-channel spectra. For instance, Luo et al. [28] conducted global dust monitoring by employing multiple channels of the FY-3 satellite (near-infrared, mid-infrared, and thermal infrared split windows). Combining the 0.54 μm and 0.86 μm band ratios with BTD (11–12), Roskovensky and Liou [29] constructed the *D*-parameter method, which can effectively distinguish between dust particles and cirrus clouds.

Despite various advantages and disadvantages in previous studies on dust-related products, a notable gap persists in research related to the inversion and identification of ground dust intensity. Based on the differences in spectral and radiative characteristics between dust and other typical ground objects, this study introduces a novel method for spring dust identification, based on the Himawari-9 (H9) satellite data. This new method combines the BTD with the normalized multiple infrared dust index (MIDI) developed by Liu et al. [30]. Furthermore, by establishing dynamic background brightness temperature fields with eight observations per day, threshold statistics are applied to explore the correlation between the IDDI and ground-observed dust levels, thereby creating a satellite-based algorithm for identifying near-surface dust intensity levels. This endeavor aims to provide data support for the refinement and quantification of dust monitoring and forecasting.

## 2. Materials and Methods

### *2.1. Data*

The H9 satellite is equipped with the Advanced Himawari Imager (AHI), a state-of-the-art optical sensor that provides multi-spectral imagery. The AHI sensor monitors the emitted radiation and backscatter of the Earth's atmospheric system through 16 bands from 0.4 to 14 µm (visible, near-infrared, and thermal infrared), with a spatial resolution of 0.5 to 2 km [31,32]. The AHI performs full-disk scanning every 10 min, enabling the real-time tracking of dust events [33].

The land surface data used in this study were derived from the Meteorological Information Comprehensive Analysis and Processing System, an advanced human–computer interactive system for meteorological information processing and weather forecasting, developed by the China Meteorological Administration (CMA). Among the various land surface types, three of them are most relevant to dust: aeolian land, gobi, and desert. The distribution of these three land surface types in northern China is shown in Figure 1a. In the following context, gobi and desert are considered the primary land surface types for dust generation.

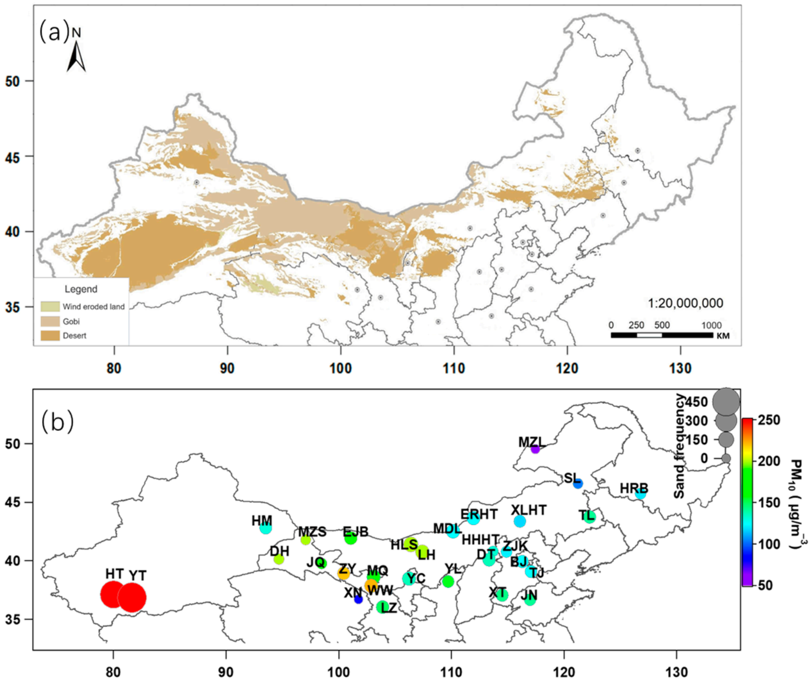

**Figure 1.** (**a**) The underlying surface type; (**b**) the frequency of dust events and the average PM10 concentration at 30 stations from March to May 2023.

The near-surface dust observation data used in this study are from the surface observation stations of CMA from March to May 2023. The dust events have five categories: floating dust (FD), blowing sand (BS), sand storm (SS), severe sand storm (SSS), and extremely severe sand storm (ESSS). According to the "National Standard of the People's Republic of China—Classification of sand and dust weather" [34], the visibility criteria for FD, BS, SS, SSS, and ESSS are <10 km, 1–10 km, <1 km, <500 m, and <50 m, respectively. In addition, FD also requires a wind force of less than or equal to 3.

The selected 30 monitoring stations are all located in northern China (as shown in Figure 1b), with 3 in Xinjiang, 10 in Inner Mongolia, 7 in Gansu, 2 in Hebei, and 1 each in Ningxia, Qinghai, Heilongjiang, Shaanxi, Shanxi, Beijing, Tianjin, and Shandong. The temporal resolution is 1 h, and the total number of samples is 56,159. The hourly $PM_{10}$ and $PM_{2.5}$ mass concentration observation data are obtained from the national control stations provided by the China National Environmental Monitoring Station website (http://www.cnemc.cn, accessed on 1 October 2023). As seen in Figure 1b, the stations with the highest frequency of dust (over 500 times) are Hetian and Yutian, located in the Taklamakan Desert in southern Xinjiang, with average $PM_{10}$ concentration exceeding 300 $\mu g \cdot m^{-3}$. At the selected stations in central and western Inner Mongolia, Gansu, Ningxia, Shaanxi, the Beijing–Tianjin–Hebei region, and Heilongjiang, the dust weather frequencies range from 41 to 137 times. Among them, the average $PM_{10}$ mass concentration in Zhangye and Wuwei in Gansu exceeds 200 $\mu g \cdot m^{-3}$, while the average $PM_{10}$ concentration in other regions ranges between 100 and 200 $\mu g \cdot m^{-3}$. In the eastern–central part of Inner Mongolia, Manzhouli, Suolun, and Xining in Qinghai, there are relatively low dust frequencies (less than 32 times), and their corresponding average $PM_{10}$ concentrations are generally below 100 $\mu g \cdot m^{-3}$.

The lidar data and L-band boundary layer wind profiles from the Jiuquan station in Gansu Province are provided by the CMA Meteorological Observation Center. The lidar data have a temporal resolution from 30 s to 30 min, a spatial resolution of 7.5 m, and an emission wavelength of 532 nm. The wind profiler radar can provide observational data every 6 min, including measurements of horizontal wind speed, wind direction, and vertical velocity. The space-borne lidar CALIOP on board the Cloud-Aerosol Lidar and Infrared Pathfinder Satellite Observation (CALIPSO) satellite provides information on aerosol types in the separate layers that can be detected with this instrument. In this study, the aerosol subtypes of CALIOP are used for dust identification verification. In regard to the H9 satellite aerosol optical depth (AOD) data, this study uses the SBDART (Santa Barbara DISORT Atmospheric Radiative Transfer) model to simulate thermal infrared atmospheric radiation. This simulation generates a lookup table of thermal infrared brightness temperature differences corresponding to different AOD values. Subsequently, the dust AOD is retrieved according to the brightness temperature difference obtained from the satellite, based on the method of Yan et al. [35].

### 2.2. Dust Identification Method

The BTD method is proposed based on the differences in the radiative properties of dust aerosols across different infrared bands. For dust aerosols, a disparity exists in the emissivity between the 11 μm and 12 μm channels in the infrared split window, typically resulting in a small or negative difference between them.

$$\mathrm{BTD} = T_{11\mu\mathrm{m}} - T_{12\mu\mathrm{m}}, \quad (1)$$

where $T_{11\mu m}$ and $T_{12\mu m}$ represent the brightness temperatures of the 11 μm channel and the 12 μm channel, respectively.

Research has shown that certain cirrus clouds can also produce small split-window brightness temperature difference. The brightness temperatures observed by satellites are directly influenced by surface temperature, emissivity, and dust properties. However, relying solely on a fixed BTD threshold for dust identification may introduce errors in dust detection [36].

Utilizing the characteristics of emissivity difference between ground and air infrared channels, Liu et al. [30] proposed an algorithm that employs the normalized MIDI to identify dust. Their statistical results indicate that the MIDI values are remarkably higher during dusty weather than under clear skies.

$$\mathrm{MIDI} = (T_{8.6\mu\mathrm{m}} + T_{12.3\mu\mathrm{m}})/(2 \times T_{11.2\mu\mathrm{m}}) \times 1000, \quad (2)$$

where $T_{8.6\mu m}$, $T_{12.3\mu m}$, and $T_{11.2\mu m}$ represent the brightness temperatures of the 8.6 μm channel, 12.3 μm channel, and 11.2 μm channel, respectively. To facilitate the distinction and setting of threshold conditions, the MIDI value is multiplied by 1000.

To align with the dust-related weather phenomenon data from ground stations, the H9 satellite grid points corresponding to 30 ground observation stations and their surrounding nine grid points ($T_{8.6\mu m}$, $T_{11.2\mu m}$, and $T_{12.3\mu m}$) are extracted for the period from March to May 2023. Spatial and hourly averages are then calculated for these extracted data.

Subsequently, a correlation analysis between the BTD and MIDI is performed based on the dust intensity level at the ground stations (Figure 2a) under different underlying surface conditions such as non-sand sources, deserts, and gobi (Figure 2b). As depicted in Figure 2a, dust data accounts for approximately 9% of the total sample data. Among the dust samples, BS and FD constitute roughly 66% and 31%, respectively, while SS and higher dust intensity levels only account for approximately 3%. As seen from the correlation between the BTD and MIDI (Figure 2a), dust samples are mainly located in the lower-right region of the entire data sample. Thus, relying solely on MIDI threshold conditions, such as setting a dust threshold above 990 or 995, can result in the misclassification of some non-dust data (highlighted in the yellow circled area). Conversely, for the BTD, if the threshold is set to less than 0 according to previous research [20], a significant number of dust samples will be missed. Moreover, adopting a more lenient threshold would substantially increase the proportion of misclassifications (highlighted in the red-circled area). Consequently, by combining the threshold conditions of the BTD and MIDI, misclassifications and missed detections can be reduced to a certain extent. Further discussions on threshold selection will be presented in subsequent sections.

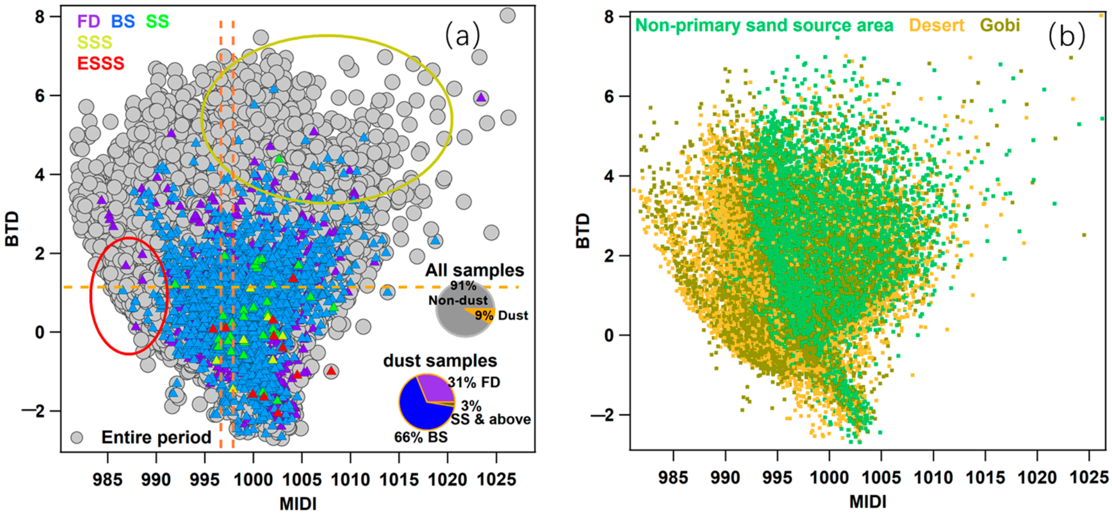

**Figure 2.** (**a**) Correlation analysis between brightness temperature difference (BTD) and multiple infrared dust index (MIDI). The gray circles represent all samples. The colored triangles represent the statistical distribution of different levels of surface dust events. (**b**) Correlation distribution for non-primary sand source, desert, and gobi. The highlighted in the red circled and yellow circled area is the misclassification of some non-dust data. The yellow dotted line represents different thresholds for MIDI and BTD.

The surface emissivity varies with land cover type, which is also a crucial factor affecting the accuracy of dust identification. Mainland China has diverse surface types, with vast deserts and gobi areas in the northwestern region that emit significant amounts of dust annually and are the primary sand sources of China. The land cover types are categorized into deserts, gobi, and non-primary sand sources (other surface types) in this study. When comparing the correlation between the BTD and MIDI for selected stations, it is noted that there is no significant difference in the BTD distribution among the three types of land cover. As for the MIDI, the distribution patterns are generally comparable for desert and gobi surface types. However, for non-primary sand source areas, the MIDI distribution tends to cluster in higher-threshold regions, generally exceeding 992. Therefore, it can be inferred that when using the MIDI for dust identification, different thresholds may be required for primary and non-primary sand source areas. Specifically, when the underlying surface is a non-primary sand source, the MIDI criteria for dust identification may need to be more stringent than those for the primary sand source areas of deserts or gobi.

The statistics of the MIDI for different dust intensity levels are presented in Figure 3a. It can be seen that, without considering the underlying surface conditions, the 25th percentile and 75th percentile of MIDI data for the entire observation period fall below 1000 and 996, respectively, with a mean of 997–998. This value is considerably lower than the MIDI statistical values for dust weather. When categorizing the underlying surface types into desert, gobi, and non-primary sand source areas, it is noted that there are fewer statistical samples over non-primary sand source areas for SSS and ESSS, which are not shown in the figure. For the same dust intensity level, the MIDI statistical values for non-primary sand source areas are generally higher than those for desert and gobi. To better utilize the MIDI for dust weather identification, statistical analyses are conducted for different dust intensity levels over the same underlying surface. The lowest 25th percentile of the MIDI for desert or gobi is 996.4 (FD), while for non-primary sand source areas, it is 997.6 (SS). These values are considered to be the dust identification thresholds for the two types of underlying surfaces. Subsequently, frequency distribution analysis of the MIDI is performed for the entire observation period and for dust weather separately. The results show that for the entire observation period (Figure 3b), the highest frequencies of the MIDI for both desert–gobi and non-primary sand source areas are mainly within 996–998. Nonetheless, the frequency distribution of the MIDI under desert-gobi conditions tends to follow a normal distribution, whereas the frequency distribution pattern of the MIDI for non-primary sand source areas skews towards values higher than 998. During dust periods (Figure 3c), the highest frequency of MIDI occurrences in desert–gobi is mainly concentrated in the range of 998–1000, followed by 1000–1002. However, the high-frequency distribution of the MIDI in non-primary sand source areas is relatively concentrated, mainly between 998 and 1004, accounting for approximately 71.2% of MIDI occurrences.

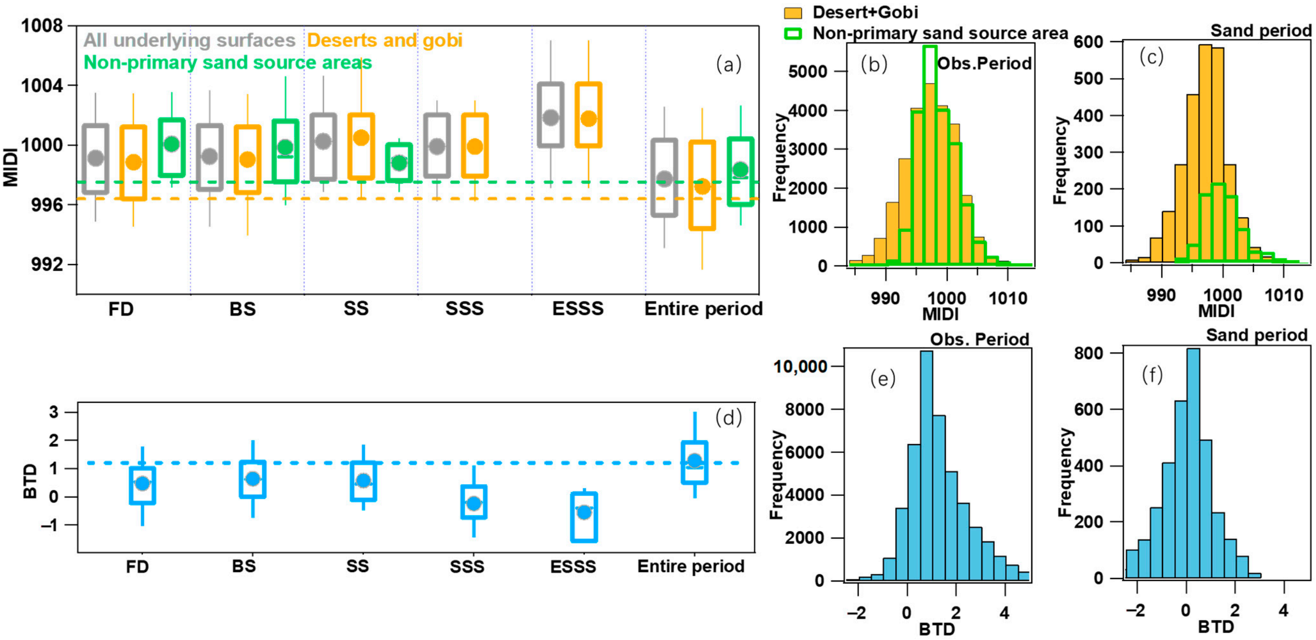

**Figure 3.** (**a**) The statistical distribution of MIDIs for different dust levels on different underlying surfaces. The frequency distribution of MIDIs under different underlying surface conditions during (**b**) the entire study period and (**c**) dust weather periods. (**d**) The statistical distribution of BTDs corresponding to different dust levels. (**e**,**f**) are the same as (**b**,**c**), but for BTD. In (**a**,**d**), the horizontal dashed lines denote the average statistical values of the corresponding underlying surfaces, the dots represent the mean values of the corresponding dust levels, the vertical lines represent the 10th percentile (lower) and 90th percentile (upper), and the horizontal lines from top to bottom represent the 25th, 50th, and 75th percentiles (same for Figure 5).

Similarly, the statistics of BTDs for different dust intensity levels are presented in Figure 3d. The statistical values of BTDs for the entire observation period are clearly higher than those during dust weather (Figure 3d), with an average value exceeding 1.28. The lowest 75th percentile of BTDs among BS, FD, SS, SSS, and ESSS (1.25) is adopted as the BTD identification threshold for dust weather. Additionally, frequency distribution analysis of the BTDs is conducted for the entire observation period and dust weather separately. As there is no significant difference in the distribution of BTDs under the two types of underlying surfaces (as shown in Figure 3e,f), the underlying surface is not distinguished. During the entire observation period, over 62% of BTD occurrences are mainly located between 0 and 2, whereas during dust weather, approximately 69% of BTD values are distributed between $-1$ and 1.

In summary, when using MIDIs and BTDs for dust identification, the thresholds for underlying surfaces of gobi and desert require BTD $< 1.25$ and MIDI $> 996.4$, while for other non-primary sand source areas, the thresholds are BTD $< 1.25$ and MIDI $> 997.6$.

## 3. Results

### *3.1. Methods for Determining the Dust Level*

The IDDI is defined as the difference between the background brightness temperature of the surface and the actual brightness temperature of the target observed by the satellite [37]. It represents the attenuation of the brightness temperature of the atmosphere–surface system caused by atmospheric dust aerosols, and is commonly used as a semi-quantitative indicator of dust intensity. A higher IDDI value suggests a higher concentration of dust in the air. By constructing a clear-sky background set at 11.2 μm, the calculation of the IDDI can be achieved, so as to depict the intensity of dust weather. Due to the influence of surface background brightness temperature and meteorological factors, $T_{11.2\mu m}$ exhibits a certain diurnal variation pattern. In this study, the daily data of each pixel are divided by eight time periods: 01–03 UTC, 04–06 UTC, 07–09 UTC, 10–12 UTC, 13–15 UTC, 16–18 UTC, 19–21 UTC, and 22–24 UTC. The maximum $T_{11.2\mu m}$ value within the past 10 days during the corresponding time period is used as the clear-sky background value ($TB_{11.2\mu m}$), and is updated daily. The formula for the IDDI is: IDDI = $TB_{11.2\mu m} - T_{11.2\mu m}$. Figure 4 shows the background brightness temperature distributions from 07 to 09 UTC during the dust occurrence days from March to May 2023. As seen from the figure, there is a certain seasonal variation trend in the background brightness temperature values in most areas of northern China from March to May, with the background brightness temperature gradually increasing as solar radiation intensifies.

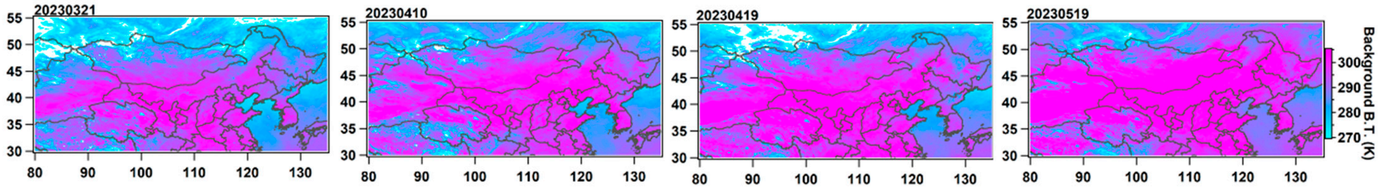

**Figure 4.** The highest background brightness temperature distributions during 07–09 UTC on dust occurrence days of 21 March 2023, 10 April 2023, 19 April 2023, and 19 May 2023.

When monitoring and forecasting dust intensity, we are concerned about the near-surface dust intensity level. To establish a correlation between the IDDI and dust intensity, a statistical analysis of the distribution trends and frequencies of the IDDI and surface $PM_{10}$ observations is conducted separately for non-primary sand source areas and desert–gobi regions, as depicted in Figure 5a,b. In non-primary sand source areas, the occurrence probability of $PM_{10}$ exceeding 600 $\mu g \cdot m^{-3}$ is relatively low, so the statistical results only display the values within 600 $\mu g \cdot m^{-3}$. To eliminate the interference of haze on dust weather, the data from selected stations where the ratio of $PM_{2.5}$ to $PM_{10}$ is higher than 55% are excluded [38]. It can be seen from the figures that under different underlying surface conditions, the IDDI exhibits a certain increasing trend as the $PM_{10}$ concentration increases. However, when the $PM_{10}$ mass concentration exceeds 600 $\mu g \cdot m^{-3}$ on desert–gobi surfaces, the increasing trend in the IDDI immediately weakens, indicating a reduced ability of the IDDI to characterize stronger intensities of dust weather in major sand source areas. With increasing $PM_{10}$ mass concentration, the increase rate of IDDIs in non-primary sand source areas is slightly slower than in desert–gobi areas. Furthermore, a statistical analysis of the correlation between $PM_{10}$ and surface dust intensity level (Figure 5c) shows that the average $PM_{10}$ concentration for the entire observation period is notably lower than the average $PM_{10}$ concentration for dust weather. It should be noted that there is no significant difference in $PM_{10}$ concentration between BS and FD (the distinction between BS and FD is primarily the wind speed), so BS and FD are not distinguished when identifying dust intensity levels with the IDDI in the subsequent analysis. The average and median $PM_{10}$ concentrations for SS, SSS, and ESSS gradually increase. The average $PM_{10}$ concentration for SDS reaches 915 $\mu g \cdot m^{-3}$, and the averages for SDS and ESDS both exceed 1000 $\mu g \cdot m^{-3}$. To further establish a relationship between the IDDI and dust intensity level (Figure 5d), the 25th percentile of the IDDI is used as the threshold for dust intensity. Grid points that have been identified as dust but with IDDI values not reaching the level of "FD and BS" are identified as "critical dust points". The specific criteria for identifying dust intensity levels with the IDDI are as follows:

IDDI: <16 critical dust

IDDI: 17–33 FD and BS

IDDI: 34–39 SS

IDDI: 40–52 SSS

IDDI: >52 ESSS

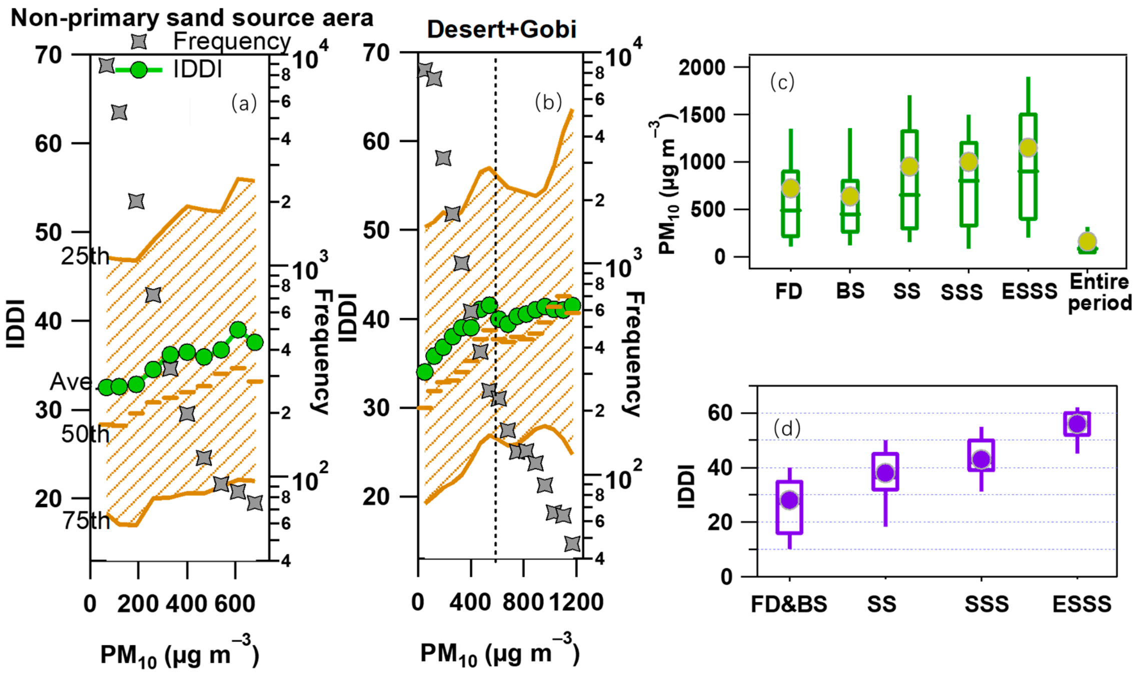

**Figure 5.** The distribution of the infrared difference dust index (IDDI) statistical values under different $PM_{10}$ ranges in (**a**) non-primary sand source areas and (**b**) desert–gobi areas, and the statistics of (**c**) $PM_{10}$ and (**d**) IDDI for different dust intensity levels.

### *3.2. Analysis of Satellite Dust Identification Results and Error Sources*

In 2023, China experienced 18 dust weather events, with 13 of them occurring from March to May. Specifically, five dust events reached an intensity of SS or above. Referring to the dates of background brightness temperature in Figure 4, we select the satellite dust level identification results at 12:00 UTC (Universal Time Coordinated) on 21 March, 09:00 UTC on 10 April, 10:00 UTC on 19 April, and 00:00 UTC on 19 May, in 2023. Then, we compare them with observations from near-surface stations. As depicted in Figure 6, at 12:00 UTC on 21 March and 09:00 UTC on 10 April, widespread dust weather occurred in southern Xinjiang, central–southern Gansu, Ningxia, and central–western Inner Mongolia, with SS and SSS observed in central Inner Mongolia. The satellite identification results align well with the ground observations in central–western Inner Mongolia, but the satellite-identified dust range in some areas of western Inner Mongolia and central Gansu are slightly larger than the ground observations. In the identification results at 00:00 UTC on 19 May, except for a certain degree of underreporting in northern Ningxia, the satellite identification and ground observations are largely consistent. At 10:00 UTC on 19 April, heavy cloud cover in the dust region of central–western Inner Mongolia significantly affects satellite dust identification. Specifically, the satellite-identified dust regions in southern Gansu and Ningxia generally match the observations, but in western Gansu, the satellite identification results indicate BS and SS in some areas where the ground observations do not indicate any dust weather.

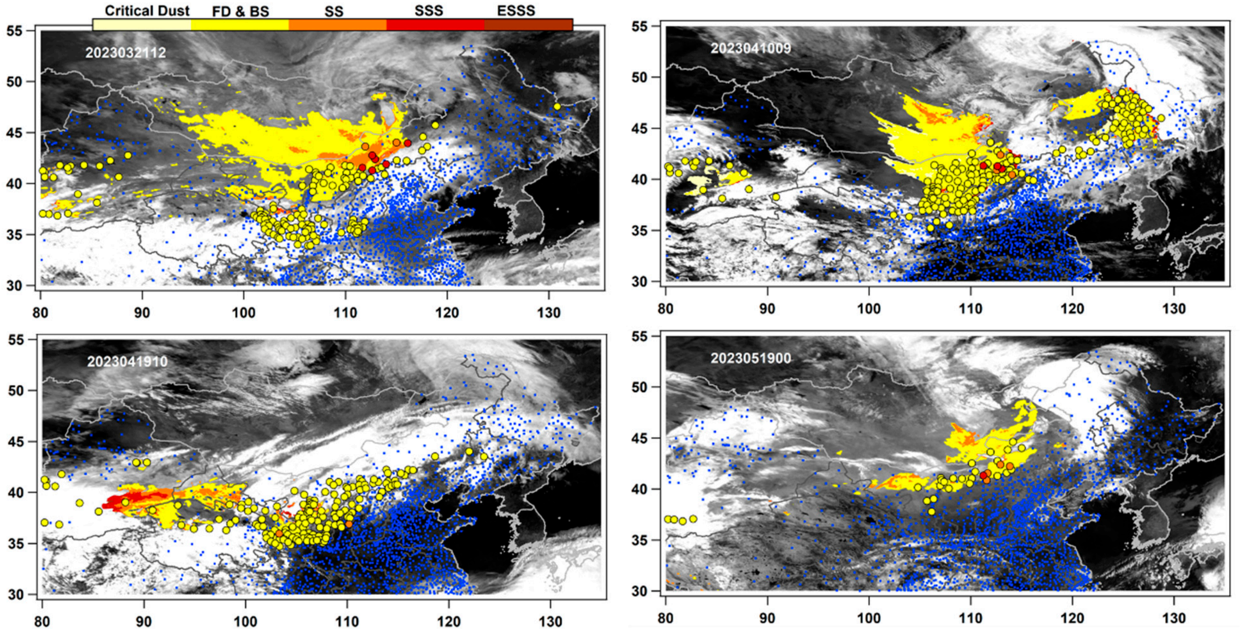

**Figure 6.** Comparison of satellite identification results of dust levels with near-surface station observations at 12:00 UTC on 21 March, 2023, 09:00 UTC on 10 April, 10:00 UTC on 19 April, and 00:00 UTC on 19 May, 2023. The black-and-white backgrounds of the figures represent the cloud images at the corresponding time. The blue dots denote the distribution of ground observation stations.

The possible reasons for the differences between satellite-identified dust range and ground observations may stem from four main factors. First, the areas with sparse ground-based monitoring stations may not fully validate the satellite identification results. Second, the uncertainties in the dust identification results may arise from the interference of clouds or the changes in the underlying surface brightness temperature caused by dust passage and nighttime temperature decreases. Third, since satellite observations cover the entire atmospheric layer, differences between ground and satellite dust observations may occur when the dust does not reach the ground during transmission. Fourth, uncertainties may also arise from the threshold selection of MIDI and BTD in satellite identification methods, as well as the identification results for the values near the thresholds. Next, we will further analyze the second and fourth factors contributing to these differences.

The ground monitoring in Sunan, Shandan, and Guaizi Lake shows that there were no dust weather events at 12:00 UTC on 21 March, but the satellite identification results indicate there was BS. At Wuwei station, the satellite identifies an SS, whereas the ground observation records BS. Furthermore, we compare the AOD (with a resolution of 1 km) from the H9 satellite 0.55 µm band. The AOD value we used is the average of nine grid points surrounding the meteorological stations (Table 1). Based on the dust identification results, at 12:00 UTC on 21 March, both satellite and ground observations detect dust at Hailisu, Wuwei, Erenhot, and Sonid Right Banner, with the lowest AOD value being 2.10. For the Guaizi Lake and Sunan stations, where the ground and satellite observations are not consistent, the AOD values are 1.85 and 1.73, respectively. Numerically, these AOD values show a certain degree of increase when compared with clear-sky conditions, but they are lower than those at the stations where dust was observed (Hailisu, Wuwei, Erenhot, and Sonid Right Banner). At this time, the average MIDI values for the nine grid points surrounding the Guaizi Lake (a desert–gobi station) and Sunan (a non-major sand source station) are 997 and 999, respectively, indicating that the MIDI values are close to the critical thresholds for dust identification. Therefore, it is speculated that there is a higher probability of misjudgment or missed detection for the points near the critical conditions of the MIDI and BTD.

**Table 1.** Comparison of AOD from six stations between 10:00 UTC and 14:00 UTC on 21 March 2023 with ground observations and satellite-based dust identification results at 12:00 UTC.

| **Date and Time 21 March 2023** | **Longitude and Latitude/Station Name** | | | | | |
|---|---|---|---|---|---|---|
| | **102.36, 41.36/ Guaizihu** | **102.87, 37.20/ Wuwei** | **99.62, 38.83/ Sunan** | **111.94, 43.61/ Erlianhot** | **112.59, 42.76/ Sunit-Right-Banner** | **106.44, 41.39/ Hailisu** |
| 10:00 | 1.99 | 2.09 | 1.99 | 5.17 | 3.54 | 2.79 |
| 11:00 | 1.85 | 1.97 | 1.87 | 4.48 | 3.92 | 2.69 |
| 12:00 | 1.80 | 2.10 | 1.73 | 4.69 | 4.82 | 2.58 |
| 13:00 | 1.85 | / | 2.05 | 3.74 | 5.29 | 3.31 |
| 14:00 | 1.77 | / | / | 4.26 | 5.04 | 2.99 |
| Ground observation at 12:00 | No dust | FD or BS | No dust | SS | SSS | FD or BS |
| Satellite identification result at 12:00 | FD or BS | FD or BS | FD or BS | SS | SS | FD or BS |

At 10:00 UTC on 19 April, satellite identification detects dust, including DS in some areas of western Gansu, but no dust events are observed at that time. According to the lidar data from the Jiuquan station (Figure 7a), from 20:00 UTC on April 18 to 04:00 UTC on 19 April, there was significant local dust weather in Jiuquan, with the dust layer mainly concentrated in the near-surface layer. The wind profiler radar (Figure 7b) shows a sharp drop in wind speed below 2000 m around 03:00 UTC, corresponding to the weakening of near-surface dust. From 05:00 UTC to 12:00 UTC, a distinct high-value band of the extinction coefficient appeared at a height of 2.4–2.9 km. This phenomenon might explain the discrepancy between the satellite-identified dust weather at 11:00 UTC and the absence of ground dust observation. Around 04:30 UTC, the wind direction at a height of around 2500 m changed from southeasterly to southwesterly, accompanied by an increase in wind speed. The true-color composite image from the H9 satellite (Figure 7c) reveals significant dust coverage over the western and southwestern regions of Jiuquan. It is speculated that the high-value band of the extinction coefficient at the height of 2.4–2.9 km at the Jiuquan station is due to the dust originating from southern Xinjiang, western Gansu, and northern Qinghai, which is lifted into the air and transported by southwesterly wind to

the Jiuquan area at an altitude of 2–3 km. During this period, the surface wind in the Jiuquan region significantly weakened. The weather observations show visibility of over 8 km and no dusty weather on the ground, yet evident dust transmission is observed overhead. The true-color composite image from the H9 satellite at 10:00 UTC (Figure 7c) clearly shows significant dust coverage over Jiuquan and its surrounding areas. Based on our comprehensive analysis, the dust weather identified by the satellite at this time is caused by high-concentration non-grounded dust in the air, which leads to the discrepancy between satellite identification and ground dust observations. In addition, the CALIOP aerosol subtype data also confirm that there is indeed the presence of non-grounded dust aerosols at a height of 2–5 km in western Gansu Province (blue box in Figure 7d). The joint application of satellite and radar observations is of significant importance for the high-precision acquisition of dust information.

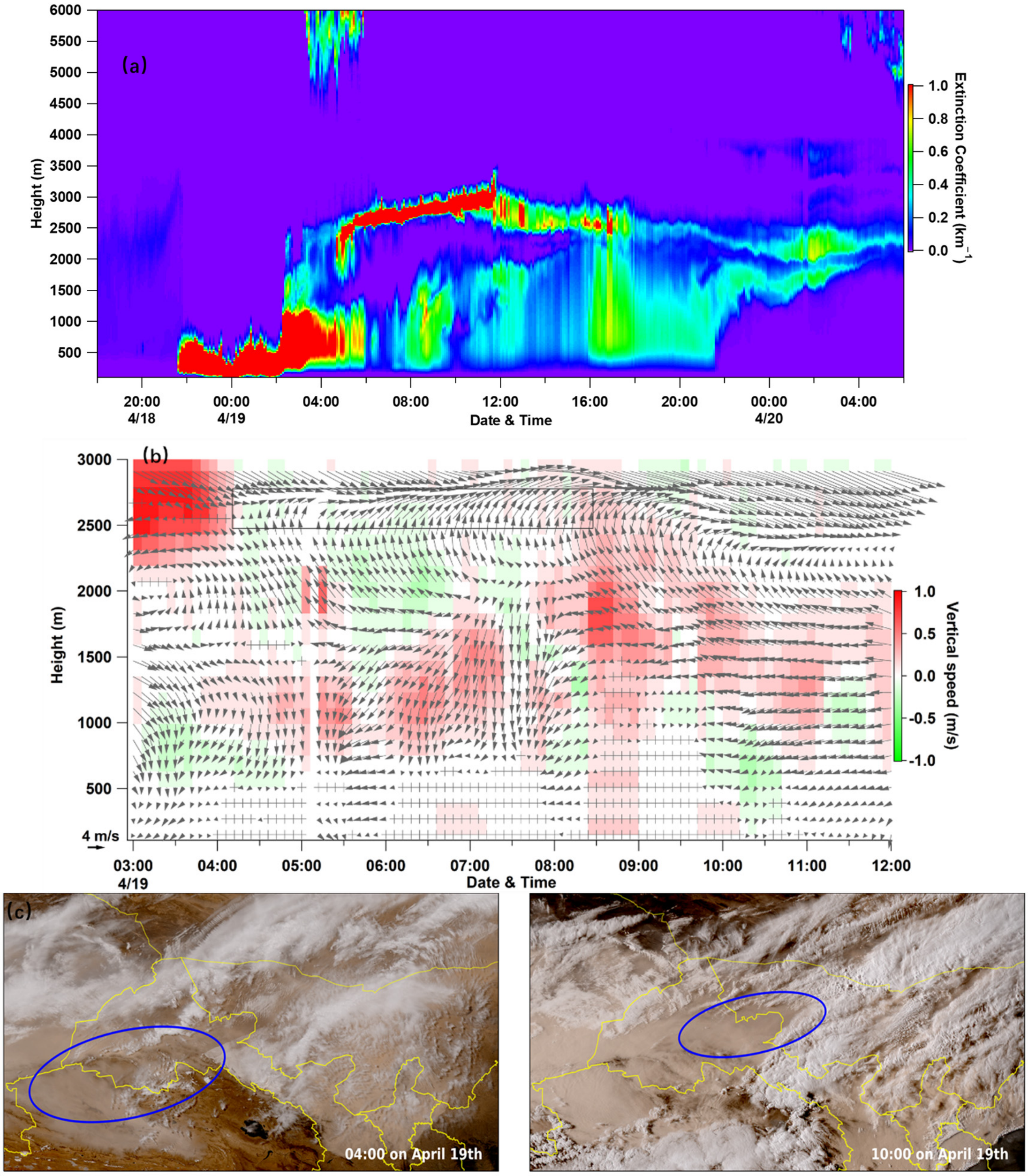

**Figure 7.** *Cont.*

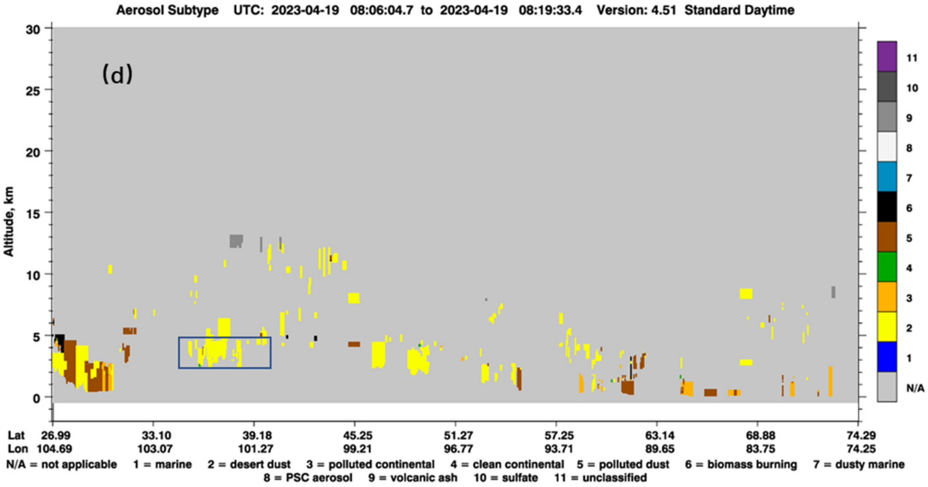

**Figure 7.** (**a**) Lidar data from Jiuquan station from 13:00 UTC on April 18, 2023, to 13:00 UTC on 20 April, 2023; (**b**) wind profiling radar data from Jiuquan station on 19 April. The direction of the arrows represents the wind direction, while the length of the arrows indicates the wind speed. The black box represents the wind field near the altitude of 2500m; (**c**) true-color composite image from H9 satellite at 12:00 UTC on 19 April and 18:00 UTC on 19 April. The blue circles represent the dust storm areas; (**d**) CALIOP aerosol subtype image from 8:06 UTC to 8:19 UTC on 19 April, 2023. The blue box indicates the area around Jiuquan at an altitude of 2–5 km.

In terms of dust intensity levels, the satellite-identified BS and FD at 12:00 UTC on 21 March are in good agreement with the ground observations. However, in the areas where the observation shows an SSS, the satellite identification results only show an SS. At 09:00 UTC on 10 April and 00:00 UTC on 19 May, the satellite identification results still underestimate the intensity of SSs or SSSs in central Inner Mongolia to some extent. According to the limited ground observations at 10:00 UTC on 19 April, the satellite identification of SSs or SSSs in southeastern Xinjiang overestimate the intensity when compared with ground observations. Hence, uncertainties still remain in the satellite-based identification of surface dust intensity levels. The main error sources in using the IDDI to determine dust intensity are as follows. Firstly, the satellite identifies dust as a full-layer phenomenon, and the samples of non-grounded dust or dust transmission at high altitudes may introduce errors when correlating IDDI statistical values with near-surface dust levels. Secondly, when a pixel is misclassified as a dust pixel during dust identification, the numerical parameters of the IDDI can lead to intensity misjudgments. Thirdly, if there are no clear-sky conditions within the past 10 days for a particular pixel when establishing the clear-sky baselines, misjudgments in dust intensity level may occur when calculating the IDDI value. The final source of error lies in the statistical correlation between IDDI values and ground weather phenomena. The use of a 25th percentile threshold value in this study has limitations, especially regarding the ability of the IDDI to accurately characterize SSSs from major dust sources, which requires further exploration. Additionally, due to the limited data sample size, there are insufficient statistical data for the SS or SSS caused by dust transmission from non-major dust source areas. This leads to considerable uncertainty in the identification of SS or higher levels of dust weather originating from non-major dust sources, which needs further research and analysis with a larger sample size.

In summary, excluding the impact of cloud cover, the satellite-based identification of dust regions is relatively accurate. However, there are still some uncertainties in determining the intensity of near-surface dust, especially when distinguishing SS and higher levels of dust events.

A comprehensive validation compares ground dust level observations with satellite identification results from 30 stations between March and May 2023. Out of 56,159 station data points, 1462 are incorrectly identified as dust, resulting in a misclassification rate of less than 3%. This result is slightly higher than the misclassification rate (9%) of dust identification obtained by using the brightness temperature difference combination threshold method proposed by She et al. [39], and is comparable to the misclassification rate (2.01%) of the improved dust aerosol identification combining CALIOP and the passive three-channel infrared imager (CLIM method) by Liu et al. [40]. Ground observations record 3470 dust occurrences, whereas satellite identification shows 1102 dust events. The majority of undetected dust events by the satellite are due to cloud cover. Among the 1102 dust events correctly identified by the satellite, the discrimination accuracy for the level of "BS and FD" exceeds 85%, while the accuracy for SS or higher levels is only around 37%.

## 4. Conclusions

Satellite remote sensing techniques can provide atmospheric pollution monitoring over wide areas, and can preserve the original characteristics of dust aerosols without their physical alteration. This capability has broad prospects in atmospheric environmental monitoring and long-distance dust transmission analysis. After analyzing the samples from the spring of 2023, it is evident that relying solely on BTD or MIDI algorithms for dust identification will cause misjudgments or missed detections of non-dust data. However, combining the threshold conditions of the BTD and MIDI can improve the accuracy of dust identification to some extent. When using MIDI for dust identification, the criteria are more stringent for non-major sand source areas than for desert or gobi. This study utilizes AHI observation data to construct a new method for spring dust identification across different underlying surface types, which can improve the accuracy of dust identification. The identification conditions for dust pixels are as follows. Desert–gobi underlying surfaces must satisfy BTD < 1.25 and MIDI > 996.4, while other non-major sand source underlying surfaces must satisfy BTD < 1.25 and MIDI > 997.6.

Furthermore, by constructing dynamic background brightness temperature values for seven times a day and performing threshold statistics on the correlation between the calculated IDDI and ground-observed dust levels, a satellite-based identification algorithm for near-surface dust intensity level is established. The test results indicate that the algorithm can effectively identify the presence or absence of dust. For dust intensity, the identification effect for BS and FD is relatively consistent with ground-based observations, but there is still significant uncertainty for SS and higher-level dust events. There are two major error sources in the algorithm. One is the difference between ground-based observations and satellite identification caused by non-grounded dust, and the other is the selection of dust identification thresholds. There are certain limitations in the thresholds for identifying dust intensity, and factors such as the underlying surface conditions and topographical features of sand sources may affect the selection of dust level thresholds. These aspects need further exploration in subsequent studies.

**Author Contributions:** Conceptualization, Q.J. and F.W.; data curation, Q.J., L.A., Y.W., Y.J. and B.L.; methodology, B.L. and J.W.; validation, J.W. and Q.J.; writing—original draft preparation, Q.J. and F.W.; writing—review and editing, Q.J., L.A. and G.W.; funding acquisition, J.W. and L.A. All authors have read and agreed to the published version of the manuscript.

**Funding:** This study was supported by the Joint Fund of the National Natural Science Foundation of China and the China Meteorological Administration (U2242209) Special Project for Weather Forecast Application under the Satellite Advancement Plan (FY-APP-ZX-2023.01), and the 2023 Innovation and Development Project of the China Meteorological Administration (CXFZ2023J009 and CXFZ2023J035).

**Data Availability Statement:** Data are available upon request from Qi jiang (jiangqi89@163.com).

**Acknowledgments:** We thank the Meteorological Observation Center of the China Meteorological Administration for providing the lidar data and wind profiler data. We also thank Nanjing Hurricane Translation for reviewing the English language quality of this paper. We also acknowledge support from the CMA Key Innovation Team (CMA2022ZD10) and the WMC Innovation Team (WMC2023IT03).

**Conflicts of Interest:** The authors declare no conflicts of interest.

## References

1. Yao, Z.; Li, J.; Han, H.; Huang, A.; Sohn, B.J.; Zhang, P. Asian dust height and infrared optical depth retrievals over land from hyperspectral longwave infrared radiances. *J. Geophys. Res. Atmos.* **2012**, *117*, D19202. [CrossRef]
2. Shao, Y.; Wyrwoll, K.-H.; Chappell, A.; Huang, J.; Lin, Z.; McTainsh, G.H.; Mikami, M.; Tanaka, T.Y.; Wang, X.; Yoon, S. Dust cycle: An emerging core theme in Earth system science. *Aeolian Res.* **2011**, *2*, 181–204. [CrossRef]
3. Jia, R.; Liu, Y.; Hua, S.; Zhu, Q.; Shao, T. Estimation of the Aerosol Radiative Effect over the Tibetan Plateau Based on the Latest CALIPSO Product. *J. Meteorol. Res.* **2018**, *32*, 707–722. [CrossRef]
4. Huang, J.; Ge, J.; Weng, F. Detection of Asia dust storms using multisensor satellite measurements. *Remote Sens. Environ.* **2007**, *110*, 186–191. [CrossRef]
5. Tu, A.Q.; Wang, Z.Z.; Zhu, G.H.; Wang, Z.F.; Zhang, H.; Zhang, S.; Liu, D.; Weng, N. Pollution characteristics of two strong dust processes in northern China in March 2021. Pollution characteristics of two strong dust processes in northern China in March 2021. *J. Arid. Meteorol.* **2023**, *41*, 607–619. (In Chinese)
6. Kato, S.; Rose, F.G.; Sun-Mack, S.; Miller, W.F.; Chen, Y.; Rutan, D.A.; Stephens, G.L.; Loeb, N.G.; Minnis, P.; Wielicki, B.A.; et al. Improvements of top-of-atmosphere and surface irradiance computations with CALIPSO-, CloudSat-, and MODIS-derived cloud and aerosol properties. *J. Geophys. Res.* **2011**, *116*, D19209. [CrossRef]
7. Chen, T.; Guo, J.; Li, Z.; Zhao, C.; Liu, H.; Cribb, M.; Wang, F.; He, J. A CloudSat Perspective on the Cloud Climatology and Its Association with Aerosol Perturbations in the Vertical over Eastern China. *J. Atmos. Sci.* **2016**, *73*, 3599–3616. [CrossRef]
8. Ham, S.-H.; Kato, S.; Rose, F.G.; Sun-Mack, S.; Chen, Y.; Miller, W.F.; Scott, R.C. Combining Cloud Properties from CALIPSO, CloudSat, and MODIS for Top-of-Atmosphere (TOA) Shortwave Broadband Irradiance Computations: Impact of Cloud Vertical Profiles. *J. Appl. Meteorol. Clim.* **2022**, *61*, 1449–1471. [CrossRef]
9. Lau, W.K.M.; Sang, J.; Kim, M.K.; Kim, K.M.; Koster, R.D.; Yasunari, T.J. Impacts of Snow Darkening by Deposition of Light-Absorbing Aerosols on Hydroclimate of Eurasia During Boreal Spring and Summer. *J. Geophys. Res. Atmos.* **2018**, *123*, 8441–8461. [CrossRef]
10. Barkley, A.E.; Olson, N.E.; Prospero, J.M.; Gatineau, A.; Panechou, K.; Maynard, N.G.; Blackwelder, P.; China, S.; Ault, A.P.; Gaston, C.J. Atmospheric Transport of North African Dust-Bearing Supermicron Freshwater Diatoms to South America: Implications for Iron Transport to the Equatorial North Atlantic Ocean. *Geophys. Res. Lett.* **2021**, *48*, e2020GL090476. [CrossRef]
11. Maki, T.; Lee, K.C.; Pointing, S.B.; Watanabe, K.; Aoki, K.; Archer, S.D.; Lacap-Bugler, D.C.; Ishikawa, A. Desert and anthropogenic mixing dust deposition influences microbial communities in surface waters of the western Pacific Ocean. *Sci. Total Environ.* **2021**, *791*, 148026. [CrossRef] [PubMed]
12. Prospero, J.M.; Barkley, A.E.; Gaston, C.J.; Gatineau, A.; Campos y Sansano, A.; Panechou, K. Caracterizing and quantifying African dust transport and deposition to South America: Implications for the phosphorus budget in the Amazon Basin. *Glob. Biogeochem. Cycles* **2020**, *34*, e2020GB006536. [CrossRef]
13. Zhang, X.Y.; Arimoto, R.; An, Z.S. Dust emission from Chinese desert sources linked to variations in atmospheric circulation. *J. Geophys. Res. Atmos.* **1997**, *102*, 28041–28047. [CrossRef]
14. Qu, J.; Hao, X.; Kafatos, M.; Wang, L. Asian Dust Storm Monitoring Combining Terra and Aqua MODIS SRB Measurements. *IEEE Geosci. Remote Sens. Lett.* **2006**, *3*, 484–486. [CrossRef]
15. Ciren, P.; Kondragunta, S. Dust aerosol index (DAI) algorithm for MODIS. *J. Geophys. Res. Atmos.* **2014**, *119*, 4770–4792. [CrossRef]
16. Yue, H.; He, C.; Zhao, Y.; Ma, Q.; Zhang, Q. The brightness temperature adjusted dust index: An improved approach to detect dust storms using MODIS imagery. *Int. J. Appl. Earth Obs. Geoinform.* **2017**, *57*, 166–176. [CrossRef]
17. Klüser, L.; Schepanski, K. Remote sensing of mineral dust over land with MSG infrared channels: A new Bitemporal Mineral Dust Index. *Remote Sens. Environ.* **2009**, *113*, 1853–1867. [CrossRef]
18. Zhang, P.; Lu, N.-M.; Hu, X.-Q.; Dong, C.-H. Identification and physical retrieval of dust storm using three MODIS thermal IR channels. *Glob. Planet. Chang.* **2006**, *52*, 197–206. [CrossRef]
19. Li, B.; Lu, S.; Sun, X.; Gao, J.; Meng, X.; Zhao, Y.; Lyu, D. Dust detection algorithm based on the entropy of visible band brightness and brightness temperature difference. *J. Remote Sens.* **2018**, *22*, 647–657. [CrossRef]
20. Legrand, M.; Plana-Fattori, A.; N'Doumé, C. Satellite detection of dust using the IR imagery of Meteosat: 1. Infrared difference dust index. *J. Geophys. Res. Atmos.* **2001**, *106*, 18251–18274. [CrossRef]
21. Ackerman, S.A. Remote sensing aerosols using satellite infrared observations. *J. Geophys. Res. Atmos.* **1997**, *102*, 17069–17079. [CrossRef]
22. Jafari, R.; Malekian, M. Comparison and evaluation of dust detection algorithms using MODIS Aqua/Terra Level 1B data and MODIS/OMI dust products in the Middle East. *Int. J. Remote Sens.* **2015**, *36*, 597–617. [CrossRef]
23. Yang, Y.; Sun, L.; Zhu, J.; Wei, J.; Su, Q.; Sun, W.; Liu, F.; Shu, M. A simplified Suomi NPP VIIRS dust detection algorithm. *J. Atmos. Sol.-Terr. Phys.* **2017**, *164*, 314–323. [CrossRef]
24. Park, S.S.; Kim, J.; Lee, J.; Lee, S.; Kim, J.S.; Chang, L.S.; Ou, S. Combined dust detection algorithm by using MODIS infrared channels over East Asia. *Remote Sens. Environ.* **2014**, *141*, 24–39. [CrossRef]
25. Zhang, H.; Xu, H.; Han, D.; Zheng, F.; Zhang, W. Dynamic dust detection method based on geostationary meteorological satellite. *Remote Sens. Inf.* **2018**, *33*, 36–44. (In Chinese)

26. Karimi, N.; Moridnejad, A.; Golian, S.; Samani, J.M.V.; Karimi, D.; Javadi, S. Comparison of dust source identification techniques over land in the Middle East region using MODIS data. *Can. J. Remote Sens.* **2012**, *38*, 586–599. [CrossRef]
27. Hao, X.; Qu, J.J. Saharan dust storm detection using moderate resolution imaging spectroradiometer thermal infrared bands. *J. Appl. Remote Sens.* **2007**, *1*, 013510. [CrossRef]
28. Luo, J.N.; Xu, Z.; Qi, Y.G. Global Dust Remote Sensing with the FengYun-3 Satellite. *J. Desert Res.* **2015**, *35*, 690–698. (In Chinese)
29. Roskovensky, J.K.; Liou, K.N. Differentiating airborne dust from cirrus clouds using MODIS data. *Geophys. Res. Lett.* **2005**, *32*, L12809. [CrossRef]
30. Liu, Q. A Method and System for Identifying Sand-Dust Regions Based on Infrared Channels in Infrared Multi-spectral Images. Chinese Patent 202211573685.X, 12 April 2023. (In Chinese).
31. Bessho, K.; Date, K.; Hayashi, M.; Ikeda, A.; Imai, T.; Inoue, H.; Kumagai, Y.; Miyakawa, T.; Murata, H.; Ohno, T.; et al. An INtroduction to himawari-8/9—Japan's new-generation geostationary meteorological satellites. *J. Meteorol. Soc. Jpn. Ser. II* **2016**, *94*, 151–183. [CrossRef]
32. Yumimoto, K.; Nagao, T.; Kikuchi, M.; Sekiyama, T.; Murakami, H.; Tanaka, T.; Ogi, A.; Irie, H.; Khatri, P.; Okumura, H.; et al. Aerosol data assimilation using data from Himawari-8, a next-generation geostationary meteorological satellite. *Geophys. Res. Lett.* **2016**, *43*, 5886–5894. [CrossRef]
33. Chen, T.; Li, Z.; Kahn, R.A.; Zhao, C.; Rosenfeld, D.; Guo, J.; Han, W.; Chen, D. Potential impact of aerosols on convective clouds revealed by Himawari-8 observations over different terrain types in eastern China. *Atmos. Meas. Tech.* **2021**, *21*, 6199–6220. [CrossRef]
34. *GB/T 20480-2017*; Classification of Sand and Dust Weather. National Standard of the People's Republic of China: Beijing, China, 2017. Available online: https://www.cma.gov.cn/zfxxgk/gknr/flfgbz/bz/202209/t20220921_5098367.html (accessed on 4 April 2023).
35. Yan, H.; Hou, Y.Y.; Liu, G.Q.; He, Y.B. Dust Detection Using Thermal Infrared Temperature Difference. *J. Remote Sens.* **2004**, *8*, 471–474. (In Chinese) [CrossRef]
36. Baddock, M.C.; Bullard, J.E.; Bryant, R.G. Dust source identification using MODIS: A comparison of techniques applied to the Lake Eyre Basin, Australia. *Remote Sens. Environ.* **2009**, *113*, 1511–1528. [CrossRef]
37. Hu, X.Q.; Lu, N.M.; Niu, T.; Zhang, P. Operational retrieval of Asian sand and dust storm from FY-2C geostationary meteorological satellite and its application to real time forecast in Asia. *Atmos. Chem. Phys.* **2008**, *8*, 1649–1659. [CrossRef]
38. Xu, W.; Zhang, D.; Li, Y.; Chen, T.; Wu, Q. Variation of PM2.5 Concentration during Two Dust Pollution Events in Beijing. *Clim. Environ. Res.* **2016**, *21*, 78–86. (In Chinese)
39. She, L.; Xue, Y.; Yang, X.; Guang, J.; Li, Y.; Che, Y.; Fan, C.; Xie, Y. Dust Detection and Intensity Estimation Using Himawari-8/AHI Observation. *Remote Sens.* **2018**, *10*, 490. [CrossRef]
40. Liu, J.; Chen, B.; Huang, J. Discrimination and validation of clouds and dust aerosol layers over the Sahara desert with combined CALIOP and IIR measurements. *J. Meteorol. Res.* **2014**, *28*, 185–198. [CrossRef]